scientific reports

Check for updates

OPEN

In-situ copper-based metal–organic framework tailored clay synthesis for efficient pharmaceutical removal: Comprehensive adsorption and optimization studies

Elcin Tutus[1], Nergiz Kanmaz[2], Tugba Hayri-Senel[1], Pelin Demircivi[2], Gulhayat Nasun-Saygili[1] & Nalan Erdol-Aydin[1]✉

The present study focuses on solvothermal in-situ synthesis of copper-based metal–organic framework (Cu-MOF) supported montmorillonite (MMT) composites (CuMMT) with various Cu-MOF mass ratios (5%, 10%, and 20%) and examine these composites as adsorbents for adsorption of tetracycline (TC) antibiotic. CuMMT composites were characterized by performing FTIR, XRD, BET/N_2, SEM, and zeta potential analyses. The impacts of temperature, initial antibiotic concentration, contact time, and solution pH on adsorption were investigated deeply. The pseudo-second-order and Elovich kinetic models were consistent with the obtained kinetic results which proposed chemical interactions. According to the studies, the monolayer Langmuir isotherm model fits the adsorption systems rather well. TC adsorption constituted a spontaneous endothermic reaction. As a result of the adsorption experiments, 10CuMMT composite showed the highest adsorption capacity as 319.57 mg g^{-1} at a contact time of 240 min, pH 7.32 (natural pH of TC solution), at a temperature of 318 K. To enhance the TC adsorption process, the Box–Behnken experimental design was used. The optimized conditions (contact time = 200 min; solid/liquid ratio = 0.08 g L^{-1}; temperature = 318 K) enhanced TC adsorption capacity to 330.70 mg g^{-1}.

Keywords Adsorption, Tetracycline, Montmorillonite, Cu-based metal–organic framework

Widespread industrialization, and uncontrolled growth in population have put more strain on available water sources (surface/groundwater), reducing their quantity and quality[1,2]. Globalization and population growth have not only led to an increase in waste, but pharmaceuticals and personal care products (PPCPs) have also recently produced a number of emerging water contaminants, such as endocrine disruptors, pesticides, and herbicides[2]. Pharmaceuticals are one type of PPCP that can be used to treat a variety of diseases. Wastewater has been shown to include nearly every kind of pharmaceutical, the majority of which are persistent. Pharmaceutical compounds (containing several groups such as anti-epileptic, antidepressant, antibiotic, hormone, anti-inflammatory, etc.) are detected in surface waters, hospital sewage, and municipal sewage. Antibiotics in the environment appear to be spreading increasing amounts and they include a growing range of compounds, and their concentrations in some rivers across the world can be up to 300 times higher than "safe" levels[1,3–5]. The World Health Organization (WHO) states that the main danger to food safety and global health is antibiotic resistance[6]. Since environmental pollution reduces the effectiveness of antibiotics used to treat infections and diseases, more and more of these diseases are becoming harder to treat[1,3,4].

Antibiotic-removal from wastewater has been accomplished using a variety treatments like chlorination, filtration, photocatalytic degradation, coagulation and sedimentation, adsorption, photo transformation, ozonation, or processes of advanced oxidation[3–11]. Selecting an appropriate method for treating pharmaceutical

[1]Chemical Engineering Department, Chemical and Metallurgical Faculty, Istanbul Technical University, 34469, MaslakIstanbul, Türkiye. [2]Department of Chemical Engineering, Faculty of Engineering, Yalova University, 77200 Yalova, Türkiye. ✉email: erdol@itu.edu.tr

wastewater depends on factors such as wastewater characteristics, cost- effectiveness, practicality, environmental compatibility, lack of sludge production, and the absence of hazardous secondary byproducts[9,10] Among these, adsorption method has been identified as superior to the others cited because of its simple application, effective pollutant removal, and more rapid action; above all, it is easy to use in field conditions and in treatment systems[9–11]

TCs are crucial antibiotics for human medication, animal disease-preventative medicine, and agricultural feed supplements because of their wide range of activity, high efficacy, and cost-effectiveness. Over 75 percent of TCs are excreted in an active state and discharged into the environment via human and animal urine and feces, causing detrimental impacts on the ecological system and human health[12].

TCs have long been challenging to efficiently remove from aqueous solutions due to their inherent physicochemical properties, stable chemical structures, non-biodegradable characteristics, and low concentrations in environmental matrices[13]. Numerous traditional techniques exist for the elimination of TCs from wastewater, including biological treatment[14], membrane separation[15], electrochemical methods[16], photocatalysis[17], ion exchange[18], and advanced oxidation processes (AOP)[19]. Still, most of these old-fashioned techniques need a lot of energy and have intricate, multi-step operating procedures. Adsorption has recently shown itself to be a successful substitute in this area because of its straightforward and uncomplicated operation, cost-effectiveness, environmental friendliness, and effective sustainability. Moreover, adsorption is frequently recognized for its efficacy at low concentrations and does not generate detrimental by-products as secondary pollutants throughout the process[3,5,11,13].

Environmental remediation (e.g., treating air and water pollution), environmental decontamination (e.g., sterilization, disinfection, separation, etc.), and environmental substitution (to replace adsorbent materials with high environmental load) are all uses for clay minerals. They may be successfully reconstructed through ion exchange because of their complex and controllable structure, which offers a high economic value and a variety of applications. In wastewater treatment, clay minerals have a special function as adsorbents[20]. MMT is a common 2:1 layered silicate clay mineral made up of two layers of silicon oxide tetrahedral layers and an interlayer of aluminum oxide octahedral layers. It is also a remarkable adsorbent due to its high specific surface area and ion exchange capacity. MMT's layered structure allows for the adsorption of a variety of compounds both on the surfaces and in the interlayer spaces, and chemical modifications of natural clay may be used to create different MMT-related adsorbents[21–23] with specific features. The interlayer space accounts for about 90% of the entire clay surface and allows MMT to absorb water molecules and other compounds[24,25]. Po-Hsiang et al.[26] studied the adsorption of TC adsorption from an aqueous solution by different montmorillonite types at varying pH, temperature, and ionic strength levels. They reported that four different smectite materials (SAz-1, SWy-2, SYn-1, and SHCa-1) had a maximum TC adsorption capacity of 468, 404, 243, and 375 mg g^{-1}, respectively.

MOFs are an unequaled type of porous crystalline materials with homogeneous and infinite coordination networks. MOFs, which are made up of metal ions or clusters coordinated with a variety of organic linkers, have a wide range of pH stability, high surface area, topologically diverse structures, and many sites for structural modification.[8,13]. Additionally, the effectiveness of these MOF-based adsorbents for the adsorptive removal of several classes of antibiotics has been further improved by the successful composite synthesis with carbon nanotubes[27], graphene oxides[28], nanoparticles[29], etc. Different pore sizes, large surface area, and simplicity of synthesis are characteristics of copper-metal organic frameworks[30]. To detect TC in aqueous solution, Nehra et al. synthesized two Cu-based metal–organic frameworks (Cu-btc) with the same stoichiometry under various reaction conditions. They found that TC-Cu^{2+} complexes are formed because tetracycline contains many O- and N-functional groups[31].

In this study, Cu-MOF supported MMT composites were synthesized at three different mass ratios of Cu-MOF (5CuMMT, 10CuMMT, and 20CuMMT), and TC adsorption performances of these composites were compared. The characterization of CuMMT composites were investigated using FTIR, XRD, BET, SEM and zeta potential techniques. The effect of the initial concentration of TC, solution pH, contact time, and temperature were examined. The data was analyzed using various isotherm and kinetic models. To enhance the TC adsorption, the Box–Behnken experimental design method was applied to assess the impact of parameters such as contact time, solid/liquid ratio, and temperature.

Notably, the CuMMT composite synthesized in this study represents a novel adsorbent material in the context of environmental remediation. No prior studies have investigated the application of a Cu-MOF/MMT hybrid structure for the removal of TC from aqueous solutions. Given the promising adsorption performance of both metal–organic frameworks and clay-based materials in pharmaceutical contaminant removal reported in recent literature, the integration of these two components is anticipated to yield a synergistic structure with enhanced functionality. Therefore, this research not only introduces a new adsorbent to the field but also lays the groundwork for further investigations into MOF-clay hybrid materials as effective and versatile platforms for emerging contaminant remediation.

Materials and methods

Materials

Tetracycline antibiotic ($C_{22}H_{24}N_2O_8$; 98%Purity) used as a target pollutant was purchased from Thermo Scientific, USA. MMT used for adsorption studies was purchased from Alya Mineral Health Training in Turkey. Copper(II) nitrate trihydrate ($Cu(NO_3)_2{\cdot}3H_2O, \geq 98\%$), terephthalic acid ($(C_6H_4(CO_2H)_2), \geq 98\%$) and N,N,dimethylformamide (DMF, ≥ 99.8%) used to obtain MOF were received from Merck Chemicals. Sodium hydroxide (NaOH, ≥ 99%), hydrochloric acid (HCl, 37%), and ethyl alcohol (C_2H_6O, 99.90%) were also obtained from Merck, Germany.

In-situ synthesis of CuMMT composites

$Cu(NO_3)_2{\cdot}3H_2O$ was weighted into a beaker in quantities corresponding to 5%, 10%, and 20% of the mass of MMT, respectively. Terephthalic acid was weighed and added as 0.25 g, 0.5 g, and 1 g into the beakers for 5CuMMT, 10CuMMT, and 20CuMMT composites, respectively. As the amount of terephthalic acid increased, the volumes of DMF and ethyl alcohol also increased. The powder mixtures were supplemented with 12.5 mL, 25 mL, and 50 mL of DMF, and with 6.25 mL, 12.5 mL, and 25 mL of ethyl alcohol, respectively. The mixtures were mixed until a distinct blue solution was achieved. Ultimately, 5 g of MMT was transferred to each beaker, and stirred for two hours.

CuMMT suspensions were placed in Teflon containers and treated trough solvothermal technique at 120 °C for 12 h. After the treatment, the solid product was separated by using filter paper with a 0.45 µm pore diameter. To get rid of the unreacted terephthalic acid, they were washed several times with DMF-ethyl alcohol, then rinsed with distilled water, and dried for 24 h at 60 °C in a drying oven.

Batch experiments

To identify the optimum TC initial concentration for adsorption experiments, conduct adsorption isotherm studies, and choose the adsorbent with the highest adsorption capacity for TC among the synthesized 5CuMMT, 10CuMMT, and 20CuMMT composites, adsorption experiments were conducted. The adsorbent amount (5 mg), contact time (24 h), TC solution volume (50 mL), and mixing speed (150 rpm) were all held constant while the adsorption studies were conducted at various TC concentrations (10–60 mg L^{-1}).

To investigate the effects of contact time, pH, and temperature on TC adsorption, a series of batch experiments were conducted using selected CuMMT composite under controlled conditions. For the kinetic and equilibrium studies, a fixed amount of adsorbent (5 mg) was introduced into 50 mL of 50 mg L^{-1} TC solution, and the mixture was stirred at 150 rpm for 5 h at room temperature.

To assess the influence of pH, experiments were performed at six different pH levels (ranging from 2 to 12), with all other parameters (adsorbent dosage (5 mg), TC concentration (50 mg L^{-1}), and solution volume (50 mL) kept constant. The pH of the solutions was adjusted using 0.2 M HCl or 0.2 M NaOH, and samples were stirred at 150 rpm for 240 min, corresponding to the established equilibrium time.

For thermodynamic analysis, the adsorption process was examined at varying temperatures (298 K, 308 K, and 318 K) under otherwise identical conditions (adsorbent dosage (5 mg), TC concentration (50 mg L^{-1}), and solution volume (50 mL)), maintaining a contact time of 240 min with continuous stirring.

The initial and residual concentrations of TC were quantified using a UV–Vis spectrophotometer (Hach DR6000 UV–Vis) at a maximum absorbance wavelength of 357 nm.

The adsorption capacity was determined by using the following equation[11,32].

$$q_e = \frac{C_0 - C_e}{W} \times \mathrm{V}$$

qe is the amount of TC adsorbed per unit weight of CuMMT (mg g^{-1}). W is the amount of CuMMT (g). C_0 is the initial TC concentration (mg L^{-1}) and C_e is the concentration of TC in solution at equilibrium time (mg L^{-1}), V is the solution volume (L).

Characterization

The BrukerTM D8 Advanced Series powder diffractometer was used to carry out the X-ray diffraction analysis. Patterns were recorded at 1.54 Å wavelength, 2θ degrees, and 0.05 Å degrees per scan speed. Data was gathered between 10° and 90° degrees. Furthermore, the Perkin Elmer FT-IR Spectrum One was used to obtain the Fourier transfer infrared spectrum (FTIR) in the 400–4000 cm^{-1} region. Brunauer Emmett-Teller (BET) measurements of N_2 adsorption isotherms were used to analyze the samples' specific surface area using the Quantachrome Quadrasorb SI instrument. The Malvern Nano ZS device was used to identify the point of net zero charge, or zeta potential.

Experimental design

Response surface methodology (RSM), a well-known technique in the design of experiments, is applied in a number of areas, including welding, material preparation conditions, removal of pollutants, etc. A well-liked design in the RSM approach, the Box–Behnken design has numerous engineering benefits. The experiment can be completed more rapidly and with significantly lower testing expenses when experimental design models are used. Besides, one area of interest for laboratory researchers is experiment design, which aims to create the ideal conditions for the best results[32]. The Box–Behnken design achieves the best results for a three-factor RSM challenge[33]. Temperature, solid/liquid ratio, and contact time were selected as factors in this investigation. The three levels were referred to as high (1), middle (0), and low (1), while the factors were named A (contact time), B (solid/liquid ratio), and C (temperature).

Results and discussion

Characterization

Figure 1a shows XRD diagrams of 5CuMMT, 10CuMMT, and 20CuMMT composites before adsorption. The diffraction peaks observed at 2θ = 19.61°, 27.92°, 35.09°, and 60.25° correspond to the MMT's main mineral component[34]. The peak observed at 2θ = 61.9° indicates that montmorillonite has a dioctahedral structure[35]. The XRD diagrams in Fig. 1a showed that MMT's main mineral component peaks at '2θ = 19.75°, 27.76°, 36.40°, and 61.93°' for the 5CuMMT composite, '2θ = 19.67°, 27.60°, 36.40°, and 62.03°' for the 10CuMMT composite, and '2θ = 19.67°, 27.71°, 36.35°, and 61.98°' for the 20CuMMT composite. The peaks at 2θ = 61.93° for the

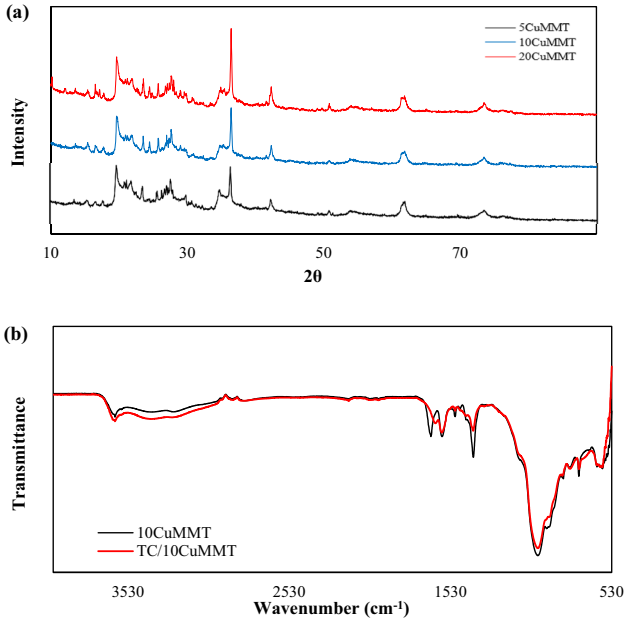

Fig. 1. (**a**) XRD patterns of samples, and (**b**) FTIR spectra of before and after TC adsorption for 10CuMMT.

5CuMMT composite, 62.03° for the 10CuMMT composite, and 61.98° for the 20CuMMT composite indicate the dioctahedral structure of montmorillonite. Abdelmoaty et al.[36] obtained particular peaks at approximately 2θ = 7°, 13.8°, 15.7°, 19.6°, 30.0°, 37.0°, 42.5°, 62.5° and 74° for the Cu-MOF. The observed peaks at 2θ = 13.66°, 15.63°, 19.80°, 29.76°, 36.51°, 42.36°, 62.06°, and 73.77° for 5CuMMT composite, at 2θ = 13.84°, 15.52°, 19.80°, 29.91°, 36.53°, 42.26°, 62.08°, and 73.85° for 10CuMMT composite, and at 2θ = 13.84°, 15.52°, 19.80°, 29.91°, 36.53°, 42.26°, 62.08°, and 73.85° for 20CuMMT can be attributed to Cu-MOF in the composite structure.

Figure 1b shows FTIR spectra from before and after TC adsorption on 10CuMMT. In the study by El Ouardi et al.[34], while the broadband at 3618 cm^{-1} was attributed to the –OH stretching vibration of MMT's structural hydroxyl groups, the broadband at 3448 cm^{-1} was attributed to the water molecules present in the interlayer. The band at 1643 cm^{-1} is assigned to the adsorbed water's bending vibration. The strong peak at 1010 cm^{-1} is assigned to Si–O stretching vibrations, indicating the presence of numerous silanol (Si–OH) groups on the montmorillonite clay surfaces. In this case, the FTIR spectrum of the 10CuMMT in Fig. 1b showed that the broadband at 3593.70 cm^{-1} can be attributed to the –OH stretching vibration of MMT's structural hydroxyl groups present in the composite, and the broadband at 3252.84 cm^{-1} can be attributed to the water molecules present in the interlayer. The band observed at 1651.25 cm^{-1} can be assigned to the adsorbed water's bending vibration. The strong peak at 991.71 cm^{-1} is assigned to the stretching vibrations of Si–O, indicating the presence of numerous silanol (Si–OH) groups on the surfaces of MMT clay.

Abdelmoaty et al.[36] observed a peak between 663 and 766 cm^{-1}, which was attributed to the aromatic ring of terephthalic acid. According to the study, the absorption band at 1390 cm^{-1} corresponding to the aromatic C=C was identified. Furthermore, three absorption bands were detected at 970, 1500, and 1640 cm^{-1}, corresponding to the vibrations of the C–O, –C=C–, and C=O groups of terephthalic acid, respectively. The appearance of three bands in the IR graphs was attributed to the effective Cu-MOF preparation. The FTIR spectrum of the 10CuMMT in Fig. 2 showed that the peak noticed at 734.26 cm^{-1} can be attributed to terephthalic acid's aromatic ring. The band characterizing the aromatic C=C is associated with the peak obtained at 1388 cm^{-1}. The three adsorption bands observed at 952.18 cm^{-1}, 1500.83 cm^{-1}, and 1582 cm^{-1} can be attributed to the vibration of C–O, –C=C– and C=O groups of terephthalic acid, respectively. The appearance of these three bands in the IR graph can be assigned to the successful synthesis of Cu-MOF. The bands obtained in the FTIR spectrum of 10CuMMT/TC in Fig. 1b correspond mainly to adsorbed TC or TC interacting with 10CuMMT since the spectrum of 10CuMMT shows much sharper and more distinct bands in the IR region studied.

BET method was used to determine the specific surface area (S_{BET}), pore size, and pores volumes. Figure 2a,b shows the isotherm and the pore size distribution curves, respectively. IUPAC classifies pores as macropores > 50 nm, mesopores 2.0–50 nm, and micropores < 2.0 nm[37]. Adsorption mostly generated mesopores at low pressure and macropores at high pressure, whereas the volume of adsorbed N_2 increased with rising P/P_o. The pore size distribution curve shows that 10CuMMT has mostly mesopores. The N_2 adsorption–desorption curve matches IUPAC type II more closely[38]. The type II isotherm is typically observed in hierarchical porous substances with micro, meso, and macroporosity, with significant porosity variation over the sample[39]. 10CuMMT has a surface area of 28.26 $m^2\ g^{-1}$, a total pore volume of 0.08 $cm^3\ g^{-1}$, and an average pore radius of 11.81 nm. While Gülen and Demirçivi[33] determined the BET specific surface area of montmorillonite clay as 72.20 $m^2\ g^{-1}$, Abdelmoaty et al.[36] determined the BET specific surface area of Cu-MOF as 1350.00 $m^2\ g^{-1}$. The lower 10CuMMT specific surface area may be due to the addition of Cu-MOF to the interlayer spaces of the MMT.

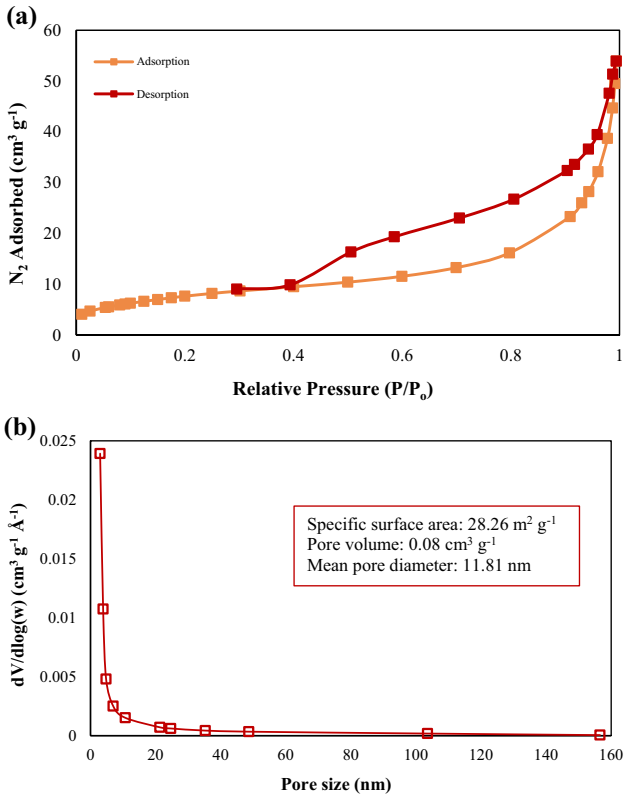

Fig. 2. (**a**) N_2 adsorption–desorption isotherm and (**b**) pore size distribution of 10CuMMT composite.

SEM images of 10CuMMT are given in Fig. 3. Fil et al.[40] confirmed that the surface morphology of montmorillonite shows a layered surface with large flakes, which is a typical structure for montmorillonite. Salama et al.[41] found that the surface morphology of Cu-BDC consists of well-formed cubic microcrystals in the SEM images obtained for Cu-BDC. In the SEM images of 10CuMMT in Fig. 3, due to the fact that the layered structures of montmorillonite are doped with Cu-MOF, the layered structures, which are typical for montmorillonite, and the cubic microcrystals of the Cu-MOF structure may not be observed.

Effect of initial TC concentration on adsorption

To examine the effect of initial TC concentration on adsorption capacity, 50 mL of TC solutions with initial TC concentrations ranging from 10 to 60 g L^{-1} were stirred for 24 h at 298 K. Adsorbent amounts were kept constant at 5 mg. The isotherm curves of the 5CuMMT, 10CuMMT, and 20CuMMT adsorbents for TC adsorption are shown in Fig. 4a. Compared to the other two adsorbents, the 10CuMMT is found to have a greater adsorption capacity for TC adsorption. For the further adsorption studies, 10CuMMT was selected as the adsorbent for removal of TC from aqueous media. The results showed that the maximum adsorption capacity of 10CuMMT for TC reached 280.55 mg g^{-1}.

Figure 4b shows the maximum adsorption capacities of 10CuMMT adsorbent for TC adsorption for different initial concentrations of TC. The adsorption capacity increased as the initial TC concentration increased. However, it was observed that as the initial concentration of TC reached over 50 g L^{-1}, the increase in adsorption capacity reduced. The TC adsorption capacity of 10CuMMT remained relatively constant. 50 g L^{-1} was used as the initial TC concentration for further adsorption studies.

Adsorption isotherms

Adsorption isotherms describe how adsorbates and adsorbents interact. The form of an isotherm provides information about the adsorption affinity of the molecule and the stability of the interaction between the adsorbent and the adsorbate[11,42]. In this study, the Langmuir, Freundlich, Temkin, and Dubinin-Redushkevich models were used to investigate adsorption equilibrium characteristics. Table 1 presents the data obtained from isotherm models for 5CuMMT, 10CuMMT, and 20CuMMT adsorbents.

The fit of the isotherm models used for TC adsorption is determined by evaluating the correlation coefficients (R^2). As a result, the Langmuir, Freundlich, and Temkin isotherm models with correlation values of 0.99 are fit for TC adsorption of 5CuMMT adsorbent. The Langmuir isotherm model is the best fit for TC adsorption of 10CuMMT and 20CuMMT adsorbents, with a correlation value of 0.99. In accordance with the findings of the literature review, the Langmuir isotherm model is better suited for TC adsorption from aqueous environments for the various adsorbents investigated[3,26,43,44].

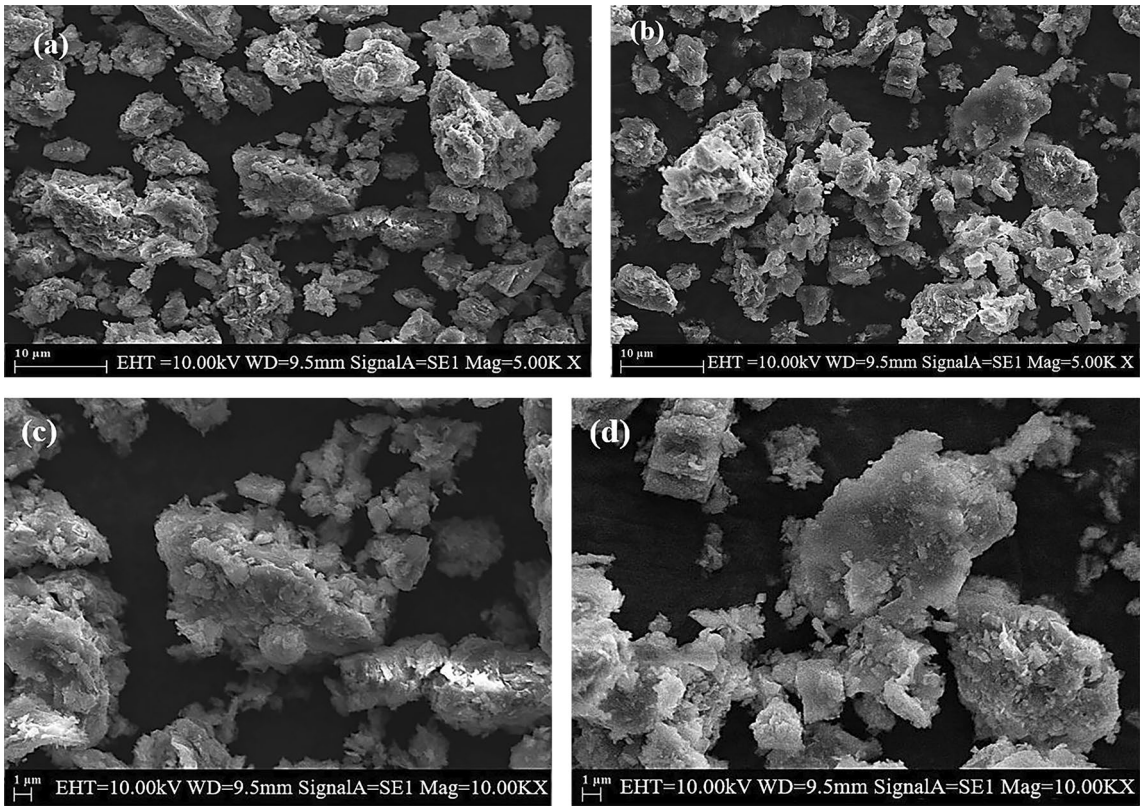

Fig. 3. (**a**,**b**) SEM images of 10CuMMT for 5 kX and (**c**,**d**) for 10 kX.

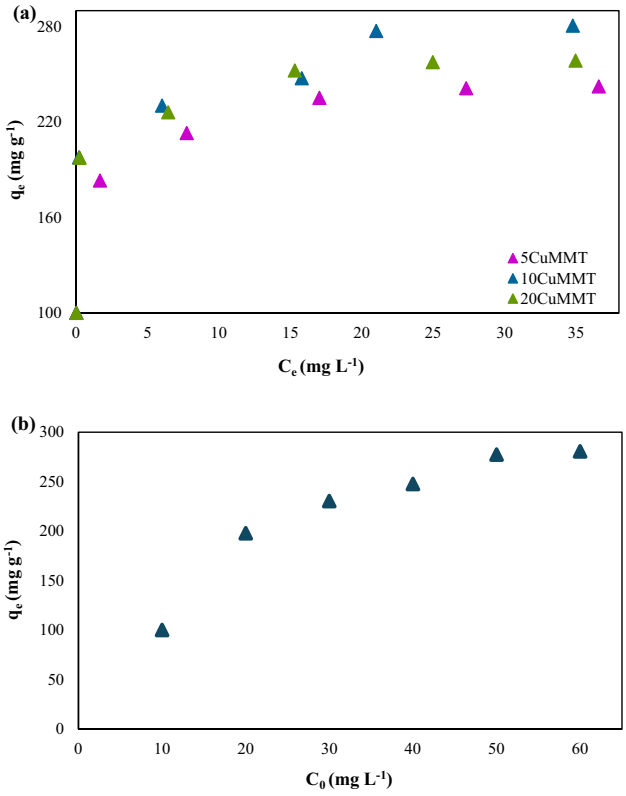

Fig. 4. (**a**) Isotherm curves for 5CuMMT, 10CuMMT, and 20CuMMT, and (**b**) effect of initial TC concentration on adsorption capacity for 10CuMMT.

Isotherm models	Parameters	5CuMMT		10CuMMT		20CuMMT	
		Value	R^2	Value	R^2	Value	R^2
Langmuir isotherm	q_{max} (mg g^{-1})	243.90	0.99	287.78	0.99	263.16	0.99
	K_L (L g^{-1})	1.78		1.50		2.92	
Freundlich isotherm	K_f (mg g^{-1})	165.64	0.99	189.16	0.89	184.23	0.88
	N	8.54		8.39		8.90	
Temkin isotherm	K_T (L g^{-1})	11,585.41	0.99	14,269.70	0.94	26,879.48	0.94
	b_T (J mol^{-1})	131.12		116.78		128.47	
Dubinin-Redushkevich isotherm	q_{max} (mg g^{-1})	222.45	0.91	253.94	0.95	244.62	0.97
	B (mol^2 J^{-2})	8×10^{-9}		9×10^{-9}		9×10^{-9}	
	E (J mol^{-1})	7905.69		7453.56		7453.56	

Table 1. Isotherm parameters of TC adsorption.

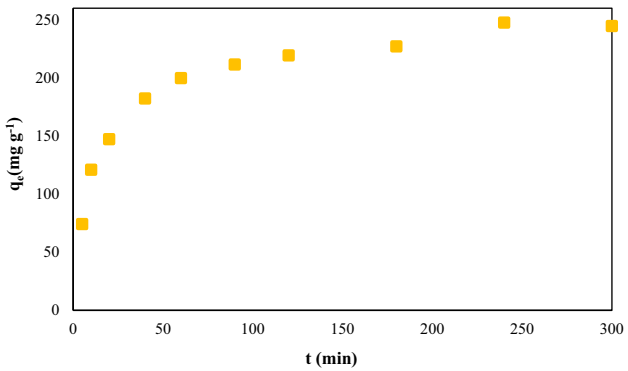

Fig. 5. Effect of contact time.

Adsorption kinetics

To study the effect of contact time on TC adsorption, 50 mL of a 50 g L^{-1} TC solution and 5 mg of 10CuMMT were stirred for 5 h at 298 K. The maximum adsorption capacities of 10CuMMT for TC adsorption at different times are shown in Fig. 5. The adsorption capacity increased as contact time increased. The adsorption capacity of 10CuMMT TC was 247.56 mg g^{-1} at 240 min and 244.64 mg g^{-1} at 300 min. After 240 min, it was observed that the adsorbent had become saturated with TC, and lower adsorption capacity was obtained at longer contact time. The time for adsorption to achieve equilibrium was determined as 240 min.

The detailed properties and mechanism of the adsorption process were clarified using pseudo-first-order, pseudo-second-order, Elovich, and intraparticle diffusion kinetic models.

Pseudo-first-order kinetic model

$$\ln(q_e - q_t) = \ln(q_e) - \frac{k_1}{2.303}t$$

q_e is the adsorption capacity of the adsorbent at equilibrium (mg g^{-1}) and q_t is the adsorption capacity of the adsorbent at time t (mg g^{-1}). k_1 represents the rate constant for pseudo-first-order adsorption (min^{-1}). The slope and interception of the graph of ln (q_e–q_t) versus t provide a linear connection from which k_1 and q_e can be calculated.

Pseudo-second-order kinetic model

$$\left[\frac{t}{q_t}\right] = \frac{1}{k_2 q_e^2} + \frac{1}{q_e}(t)$$

k_2 is the rate constant of pseudo- second-order adsorption (g mg^{-1} min^{-1}). The plot of (t/q_t) and t will give a linear relationship whose slope and intercept can be used to determine q_e and k_2 respectively.

Elovich model

$$q_t = \frac{1}{\beta} ln(\propto \beta) + \frac{1}{\beta}\ln(t)$$

α is the initial adsorption rate (mg g^{-1} min^{-1}) and β is the desorption constant (g mg^{-1}). A linear relationship with slope '(1/β)' and intercept '(1/β) ln (αβ)' can be obtained from the plot of qt versus ln (t).

Intraparticle diffusion kinetic model

$$q_t = k_{int} t^{1/2} + c$$

k_{int} (mg (g $min^{1/2})^{-1}$) is the intraparticle diffusion rate constant. The thickness of the layer that forms between the adsorbent and the adsorbed substance is determined by a constant called c. k_{int} and c values are determined using the slope and intercept of the graph obtained by plotting q_t versus $t^{1/2}$ values. Table 2 presents the data obtained from kinetics models.

When the correlation coefficients (R^2) for the kinetic models used in TC adsorption are compared, the correlation coefficient of 0.99 indicates that the pseudo-second-order kinetic model fits the data from TC adsorption of 10CuMMT adsorbent better than the other kinetic models. When the Elovich model was examined, a strong correlation coefficient of 0.98 was found. This suggests that TC adsorption on the 10CuMMT surface involves chemisorption processes[45]. The pseudo-second-order kinetic model parameter q_e value of 256.41 mg g^{-1} is closely aligned with the q_e value of 247.56 mg g^{-1} measured at 240 min. According to the literature review, numerous investigations indicate that the pseudo-second-order kinetic model more accurately describes the mechanism of tetracycline adsorption from aqueous solutions using various adsorbents[26,43,44].

Effect of pH and zeta potential measurements

The pH of the solution is a crucial factor in controlling the adsorption process. To determine the ideal pH for TC adsorption studies, 5 mg 10CuMMT and 50 mL of 50 mg L^{-1} TC solution were stirred for 240 min after adjusting the pH of the solution ranging from 2 to 12. Figure 6a shows the adsorption capacities in relation to different pH levels. TC adsorption capacity of the 10CuMMT adsorbent at acidic and neutral pH levels is slightly higher than observed in a highly alkaline media. TCs are amphoteric compounds that include numerous ionizable functional groups. The TC molecule contains three primary functional groups: tricarbonyl amide, phenolic diketone, and dimethyl amino. Depending on the pH of the solution, TCs can undergo protonation-deprotonation reactions and present many species, including the cationic form (H_3TC^+) at pH < 3.3, the zwitterionic form ($H_2TC^{\pm}$) at pH < 7.68, and the anionic form (HTC^-, TC^{2-}) at pH > 7.68[46]. Parolo et al.[47] reported that montmorillonite contains structural negative charges. The study showed that not only cationic species of TC but also neutral and monoanionic species were adsorbed on the negatively charged montmorillonite surface. They revealed that electrostatics may play an important role in the adsorption of not only H_3TC^+ but also $H_2TC^{\pm}$ and HTC^-. In the study, it was reported that the surface affinity decreased in the order of $H_3TC^+ > H_2TC^{\pm} > HTC^-$.

Zeta potential measurements are essential for comprehending the interaction between the adsorbent and the adsorbate since the adsorption process is primarily driven by electrostatic forces. A positive zeta potential indicates that the adsorbent surface promotes the adsorption of negative ions, whereas a negative zeta potential attracts positive ions to the adsorbent surface[48]. Figure 6b shows the zeta potential measurements of the 10CuMMT in the pH range of 2 to 10. The findings indicate that the 10CuMMT composite has a negative zeta potential (mV) in the pH range under consideration. In this situation, the adsorbent surface will attract positive ions. The higher TC adsorption capacity of 10CuMMT adsorbent at acidic and neutral pH is based on the attraction of cationic, zwitterionic, and monoanionic (HTC^-) forms of TC by the surface of 10CuMMT adsorbent, which has a negative zeta potential (mV). In addition, a slight decrease in TC adsorption capacity was observed at highly alkaline pH. This can be explained by the fact that the TC^{2-} anionic form of TC, which can be observed at the alkaline pH of the solution, is less attracted to the 10CuMMT surface than the cationic and zwitterionic forms.

Electrostatic attraction is not the only dominant factor in TC adsorption. Despite the adsorption capacity of the 10CuMMT adsorbent being comparatively lower in a highly alkaline pH environment than in acidic and neutral pH environments, it demonstrated a significant adsorption capacity of 221.69 mg g^{-1} in a highly alkaline pH environment.

The presence of π-electrons from the aromatic ring structure of the Cu-MOF structure in the prepared adsorbent and the aromatic ring structures of TC formed π–π interactions during the adsorption process. The aromatic rings found in TC function as acceptors for π-electrons. The presence of –COOH in the Cu-MOF structure in the adsorbent makes the benzene ring a π-electron donor. Consequently, the interplay between π-electron acceptors and donors contributed to improved adsorption efficiency through π–π interactions. Overall, the pH of the solution did not influence the π–π interactions during the TC adsorption process[49].

Kinetic models	Parameter	Value	R^2
Pseudo-first-order kinetic model	q_e (mg g^{-1})	144.68	0.88
	k_1 (dk^{-1})	0.35×10^{-1}	
Pseudo-second-order kinetic model	q_e (mg g^{-1})	256.41	0.99
	k_2 (g (mg dk)$^{-1}$)	0.25×10^{-3}	
Elovich model	α (g (mg dk)$^{-1}$)	0.43×10^{-1}	0.98
	β (g mg^{-1})	40.83	
Intraparticle diffusion kinetic model	k_{int} (mg (g $dk^{1/2})^{-1}$)	10.04	0.85
	c	96.47	

Table 2. The data obtained from kinetics models applied for TC adsorption.

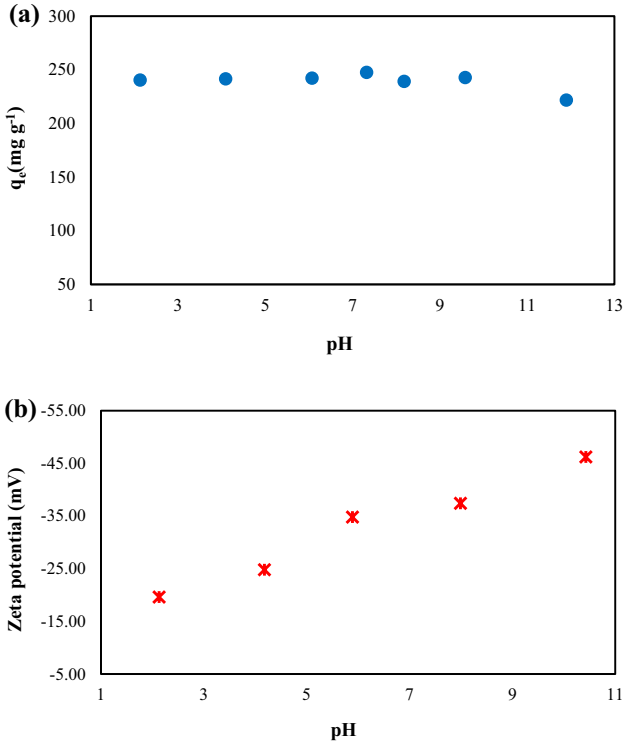

Fig. 6. (**a**) Effect of pH, (**b**) zeta potential measurements.

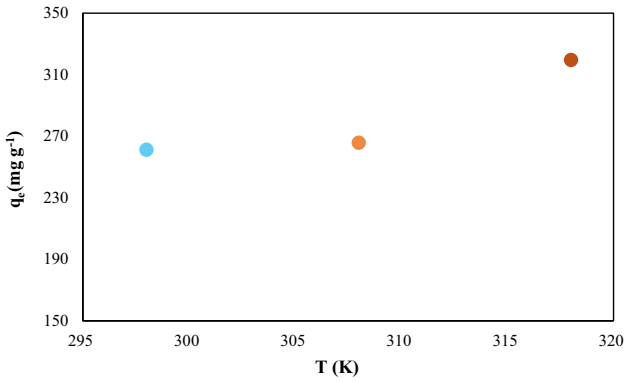

Fig. 7. Effect of temperature on adsorption.

Adsorption thermodynamics

The adsorption capacities of 10CuMMT for TC adsorption at 298 K, 308 K, and 318 K are given in Fig. 7, it shows that the adsorption capacity of 10CuMMT for TC adsorption increased as the temperature got higher. At 318 K, the adsorption capacity was higher than at the other two temperatures, and the adsorption capacity of 10CuMMT for TC adsorption was 319.57 mg g^{-1} at 318 K.

Adsorption thermodynamic parameters should be assessed to determine the feasibility and spontaneity of the process[50]. Experimental data from adsorption processes is used to calculate thermodynamic parameters, including enthalpy change (ΔH), Gibbs free energy change (ΔG), and entropy change (ΔS)[3,5,51]. The thermodynamic parameters ΔG°, ΔH°, and ΔS° were determined using Eqs. (1–5) provided below[52], with the ideal gas constant value of 8.314 J (mol K)$^{-1}$.

$$\left(\frac{dlnK}{dT}\right)_o = -\left(\frac{dlnC_e}{dT}\right)_o = \frac{\Delta H^o}{RT^2} \tag{1}$$

$$ln\left(\frac{C_{e1}}{C_{e2}}\right) = \frac{\Delta H^o}{R}\left(\frac{1}{T_2} - \frac{1}{T_1}\right) \tag{2}$$

T (K)	ΔH° (kJ mol^{-1})	ΔG° (kJ mol^{-1})	ΔS° (J (mol K)$^{-1}$)	K
298	11.09	− 5.94	57.13	10.97
308		− 6.23	56.22	11.38
318		− 7.61	58.80	17.78

Table 3. Thermodynamic parameters of TC adsorption on 10CuMMT.

S	R_2	$R_{2(adj)}$	$R_{2(pred)}$
4.07516	99.15%	97.63%	87.16%

Table 4. The summary data of the Box–Behnken model.

$$K = \left(\frac{C_{ads}}{C_e}\right) \tag{3}$$

$$\Delta G^o = -RTlnK \tag{4}$$

$$\Delta G^o = \Delta H^o - T\Delta S^o \tag{5}$$

K is the equilibrium constant, and C_{ads} is the adsorbed substance concentration (mg L^{-1}) at equilibrium. C_e is the solution's equilibrium concentration (mg L^{-1}). T is the absolute temperature (K), and R is the ideal gas constant (J (mol K)$^{-1}$). Table 3 shows the thermodynamic parameter values obtained at 298 K, 308 K, and 318 K respectively.

Table 3 shows a positive ΔH° value, indicating that 10CuMMT-TC adsorption occurs endothermically. For chemisorption, the change in enthalpy of adsorption (ΔH°) ranges between − 40 and − 80 kJ mol^{-1}, while for physisorption, it ranges between − 20 and 40 kJ mol^{-1}[53]. Thus, the enthalpy value of 11.09 kJ mol^{-1} suggests that TC adsorption is physical. Table 3 shows that the change in free Gibbs energy (ΔG°) values are negative and decrease with increasing temperature. It indicates a spontaneous adsorption process, and spontaneity increased as temperature increased. Positive ΔS° results indicate randomness at the solid-solution interface during adsorption[11,53].

Box–Behnken design and statistical assessment

Studies were conducted to investigate the effects of initial TC concentration, contact time, pH, and temperature on TC adsorption. Experimental studies indicated that changing the initial TC concentration, contact time, and temperature parameters had a significant effect on TC adsorption, however, changing the ambient pH had no major impact on TC adsorption. Contact time, solid/liquid ratio, and temperature were selected as factors for the experimental design.

The Box–Behnken experimental design was implemented using Minitab to conduct statistical analysis of the obtained data, as well as investigation, modeling, and optimization of the impacts of selected parameters. Initially, all major effects, as well as quadratic and binary interactions, were investigated. Table 4 shows model summary data for the beginning circumstance, including all terms. The statistics indicate the model's compatibility and predictive power.

According to Table 4, the R_2, $R_{2(adj.)}$, and $R_{2(pred.)}$ values are, respectively, 99.15%, 97.63%, and 87.16%. A high degree of fit is indicated by such a high R_2. A high $R_{2(adj.)}$ value suggests that there are no extraneous variables and that the model is capable of explaining the process. Furthermore, the model's predictive capability for the process is represented by the $R_{2(pred.)}$ value, which is comparatively high for this process. The fact that these numbers are so high and near to one another is agreeable. Additionally, the model's residual points exhibit low volatility, as evidenced by the standard error, or S, being as low as 4.

Table 5 lists the P-value and F-value values of the main, quadratic, and two-factor interactions of all parameters whose impacts on the process are investigated in accordance with the Box–Behnken model. First, when the overall significance of the model is examined the P-value (< 0.05) indicates that the model is significant. All of the main effects' P-values are less than 0.05, as intended, according to this analysis of the main effects. This suggests that every main factor is statistically significant. A similar problem applies to quadratic interactions. When the two-factor interactions are examined, the AC pairwise interaction is significant with a low P-value, however, the AB and BC interactions are not significant with P-values of 0.746 and 0.608, respectively. The P-value of Lack-of-Fit is > 0.05, indicating that the model generated by the design fits the data and there is no lack of fit. Despite this, since the AB and BC interactions are known to be ineffective, these interactions were eliminated from the model, and the analyses were rerun to improve the model's predictive power and accuracy.

The model summary data for the new condition is shown in Table 6. After eliminating the AB and BC interactions, all R_2 values improved, as predicted. In particular, the increase in $R_{2(pred.)}$ suggests the new model has more predictive power. Similarly, a decrease in the S value compared to the previous supports the idea that the model's accuracy has improved.

Table 7 shows the current analysis of variance results after eliminating the AB and BC interactions. The F-value and P-value of the model in the table indicate that the model is significant. The P-values for all other

Source	DF	Adj SS	Adj MS	F-value	P-value
Model	9	9739.59	1082.18	65.16	0.000
Linear	3	6238.59	2079.53	125.22	0.000
A	1	1445.83	1445.83	87.06	0.000
B	1	1855.43	1855.43	111.73	0.000
C	1	2937.33	2937.33	176.87	0.000
Square	3	3219.68	1073.23	64.63	0.000
A*A	1	574.01	574.01	34.56	0.002
B*B	1	2554.55	2554.55	153.82	0.000
C*C	1	456.01	456.01	27.46	0.003
2-Way	3	281.32	93.77	5.65	0.046
Interaction					
A*B	1	1.94	1.94	0.12	0.746
A*C	1	274.41	274.41	16.52	0.010
B*C	1	4.97	4.97	0.30	0.608
Error	5	83.03	16.61		
Lack-of-Fit	3	78.17	26.06	10.71	0.087
Pure error	2	4.87	2.43		
Total	14	9822.63			

Table 5. Analyses of variance data.

S	R_2	$R_{2(adj)}$	$R_{2(pred)}$
3.58456	99.08%	98.17%	91.68%

Table 6. The summary data of the improved Box–Behnken model.

Source	DF	Adj SS	Adj MS	F-value	P-value
Model	7	9732.69	1390.38	108.21	0.000
Linear	3	6238.59	2079.53	161.84	0.000
A	1	1445.83	1445.83	112.52	0.000
B	1	1855.43	1855.43	144.40	0.000
C	1	2937.33	2937.33	228.60	0.000
Square	3	3219.68	1073.23	83.53	0.000
A*A	1	574.01	574.01	44.67	0.000
B*B	1	2554.55	2554.55	198.81	0.000
C*C	1	456.01	456.01	35.49	0.001
2-Way	1	274.41	274.41	21.36	0.002
Interaction					

Table 7. Analyses variance data for reduced model.

effects and interactions are 0.05, suggesting that they are all significant. The P-value for Lack-of-Fit in the current case is greater than in the prior case, showing that the model is more consistent with the data and that there is no lack of fit.

The regression equation for the remaining factors is modeled as follows (Y represents the TC adsorption capacity (mg g^{-1})).

$Y = 261.11 + 13.44*A - 15.23*B + 19.16*C + 12.47*A2 + 26.30*B2 + 11.11*C2 + 8.28*A*C.$

When the coefficients in the equation are examined, it appears that factor C has the greatest effect among the main effects. The high coefficients of the squared factors suggest that the variables' nonlinear effects are also crucial for determining the optimum conditions. The most influential factor is B2, which has the highest coefficient. The fact that the AC binary interaction has a lower coefficient than the other factors indicates that it is significant, but its effect is lower than the other factors. The Pareto graph confirms all of these observations. Figure 8a shows the Pareto graph for all factors.

The three-level, three-factorial Box–Behnken experimental design was used, and the contact time (150–250 min) as factor A, solid/liquid ratio (0.08–0.12) as factor B, and temperature (298–318 K) as factor C were

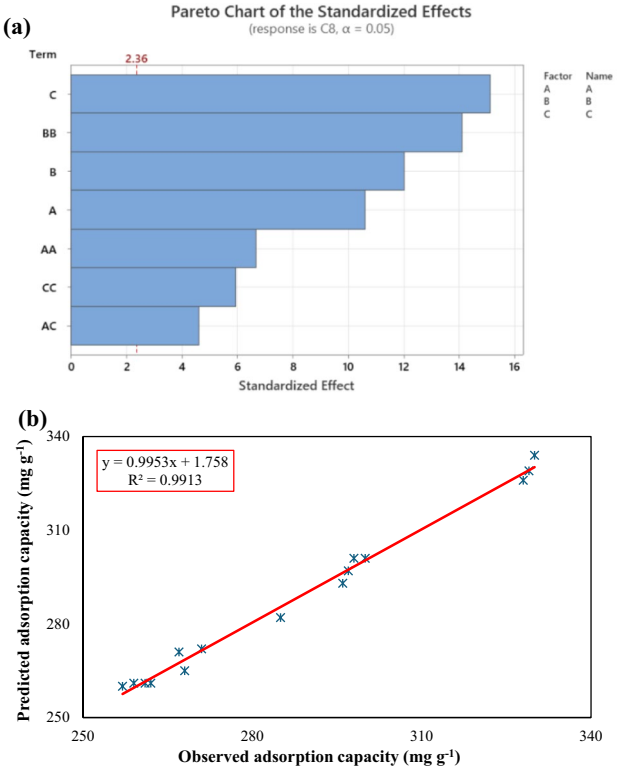

Fig. 8. (**a**) Pareto graph and, (**b**) comparison of the observed and predicted adsorption capacities.

Independent variables							TC adsorption capacity (mg g^{-1})	
	Contact time (min), A		Solid/liquid ratio, B		Temperature (K), C		10CuMMT	
Run	Coded	Actual	Coded	Actual	Coded	Actual	Observed	Predicted
1	1	250	0	0.1	1	318	328	326
2	0	200	0	0.1	0	308	261	261
3	− 1	150	0	0.1	1	318	285	282
4	0	200	0	0.1	0	308	262	261
5	− 1	150	1	0.12	0	308	271	272
6	− 1	150	− 1	0.08	0	308	300	301
7	− 1	150	0	0.1	− 1	298	257	260
8	1	250	0	0.1	− 1	298	267	271
9	1	250	1	0.12	0	308	297	297
10	1	250	− 1	0.08	0	308	329	329
11	0	200	1	0.12	1	318	298	301
12	0	200	1	0.12	− 1	298	268	265
13	0	200	− 1	0.08	1	318	330	334
14	0	200	− 1	0.08	− 1	298	296	293
15	0	200	0	0.1	0	308	259	261

Table 8. Codes of independent variables and observed and predicted TC adsorption capacities of 10CuMMT.

chosen as variable parameters. The TC concentration of 50 mg L^{-1} remained constant during the experiments. The factor levels were represented with − 1 (low), 0 (center point), and 1 (high).

The results of the TC adsorption capacity onto 10CuMMT were analyzed using the design matrix, and the obtained data are shown in Table 8. The Box–Behnken experimental design's optimized conditions (contact

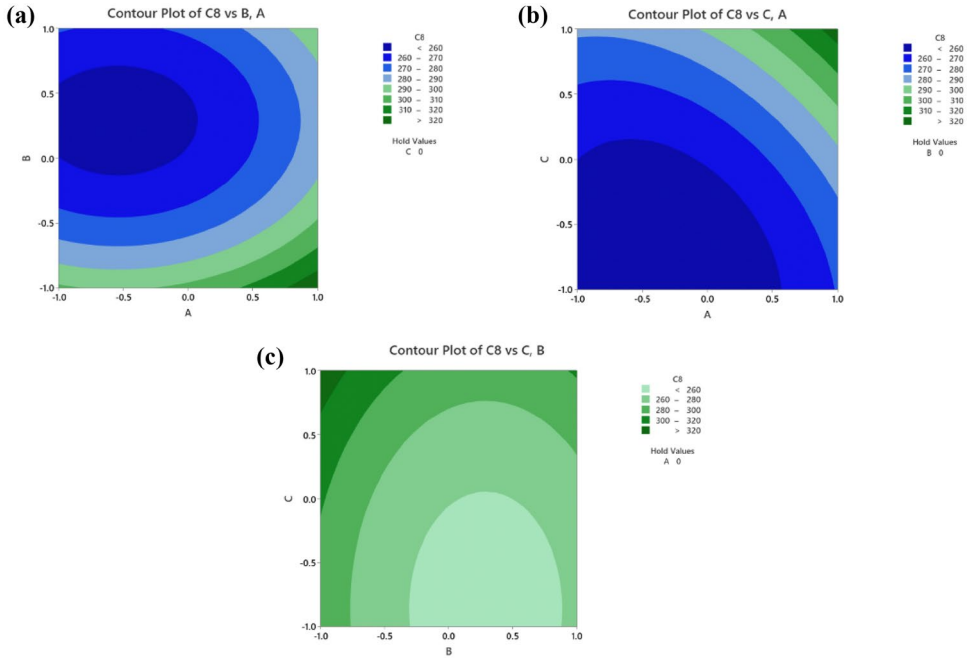

Fig. 9. (**a**), (**b**), and (**c**) Contour plots.

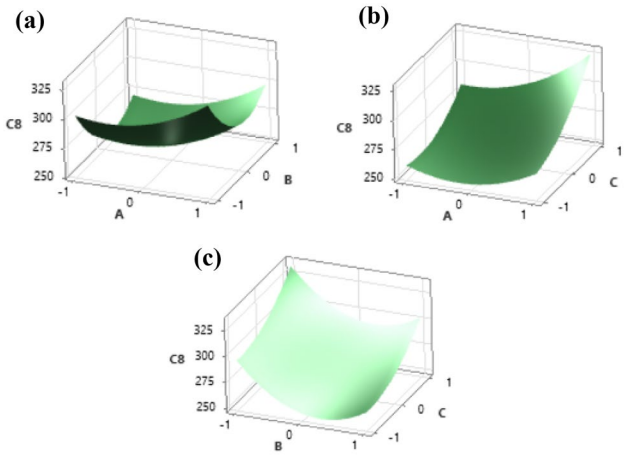

Fig. 10. (**a**), (**b**), and (**c**) Surface plots.

time = 200 min; solid/liquid ratio = 0.08; temperature = 318 K) enhanced the adsorption of TC on 10CuMMT and the maximum adsorption capacity reached 330 mg g^{-1}.

Figure 8b shows a graph of the comparison of the observed against predicted adsorption capacities. The data is noticed to be spread quite close to the trend line. This demonstrates the model's ability to make very accurate predictions. Their distribution along a certain linear line also implies that there is no systematic mistake.

Contour Plots (Fig. 9a–c) and Surface Plots (Fig. 10a–c) were used to comprehend the connections between the factors and their impacts on the dependent variable, as well as to identify the optimum points. Figures 9a and 10a show that increasing the B factor decreases the dependent variable, TC adsorption capacity (Y), while increasing the A factor increases Y values. The negative sign of the B factor's coefficient in the model equation confirms its observed negative influence on Y. It can be observed that areas with high A and low B constitute optimum zones. Figures 9b and 10b illustrate that the value of Y rises when both the A and C factors increase. Maximum values are achieved in Figs. 9c and 10c when B decreases and C increases. The change in the C factor has a considerable effect on the dependent variable Y.

Conclusion

This study found that copper-based metal–organic framework doped Montmorillonite (CuMMT) composite is an effective as a new adsorbent for the removal of TC from aqueous environment. In this study, three different

CuMMT composites (5CuMMT, 10CuMMT, and 20CuMMT) were synthesized using varying Cu-MOF ratios. The composites characterized via FTIR, XRD, BET, SEM, and zeta potential analyses, confirming successful synthesis.

Adsorption experiments were conducted to evaluate the effects of initial TC concentration, contact time, solution pH, and temperature on the adsorption behavior. 10CuMMT exhibited the highest adsorption capacity and was selected for further detailed studies. Equilibrium was reached at 240 min, and optimal adsorption was achieved at the natural pH of the TC solution (pH 7.32) and 318 K, yielding a maximum adsorption capacity of 319.57 mg g^{-1}. In addition to electrostatic interactions, π–π interactions between the aromatic rings of TC and the Cu-MOF structure also played a crucial role in the adsorption mechanism. The π-electron donor–acceptor dynamics between the Cu-MOF's –COOH functionalized benzene rings and TC's aromatic structures significantly enhanced the overall adsorption efficiency. The adsorption process conformed to the Langmuir isotherm model and pseudo-second-order kinetics, while thermodynamic analysis indicated that the process was endothermic and spontaneous.

The optimized conditions (200 min, 0.08 g L^{-1} solid/liquid ratio, and 318 K) obtained by applying Box-Behnken experimental design enhanced the TC removal, achieving an adsorption capacity of 330.70 mg g^{-1}. The study concludes that 10CuMMT is a highly promising adsorbent for the effective removal of TC from wastewater, with potential applicability in environmental remediation practices. In future studies, a comprehensive feasibility and experimental study on the potential for industrial scale application is planned and this deficiency is aimed to be addressed.

Data availability

The data presented in this study are available on request from corresponding author.

Received: 18 March 2025; Accepted: 19 May 2025
Published online: 22 May 2025

References

1. Vasilachi, I. C., Asiminicesei, D. M., Fertu, D. I. & Gavrilescu, M. Occurrence and fate of emerging pollutants in water environment and options for their removal. *Water* **13**(2), Article 2. https://doi.org/10.3390/w13020181 (2021).
2. Ahamad, A., Madhav, S., Singh, A., Kumar, A., & Singh, P. *Types of Water Pollutants: Conventional and Emerging*, 21–41. https://doi.org/10.1007/978-981-15-0671-0_3 (2019).
3. Alameri, A. A. et al. Ciprofloxacin adsorption using magnetic and ZnO nanoparticles supported activated carbon derived from *Azolla filiculoides* biomass. *Biomass Convers. Biorefinery* **14**, 27001–27014. https://doi.org/10.1007/s13399-022-03372-6 (2024).
4. Kyzasa, G. Z., Mengelizadehb, N., Salootc, M., Mohebid, S. & Balarak, D. Sonochemical degradation of ciprofloxacin by hydrogen peroxide and persulfate activated by ultrasound and ferrous ions. *Colloids Surf. A* **642**, 128627. https://doi.org/10.1016/j.colsurfa.2022.128627 (2022).
5. Balarak, D., Mahvi, A. H., Shahbaksh, S., Wahab, Md. A. & Abdala, A. Adsorptive removal of azithromycin antibiotic from aqueous solution by azolla filiculoides-based activated porous carbon. *Nanomaterials* **11**, 3281. https://doi.org/10.3390/nano11123281 (2021).
6. França, D. B. et al. The versatility of montmorillonite in water remediation using adsorption: Current studies and challenges in drug removal. *J. Environ. Chem. Eng.* **10**(2), 107341. https://doi.org/10.1016/j.jece.2022.107341 (2022).
7. Balarak, D., Mengelizadeh, N., Rajiv, P. & Chandrika, K. Photocatalytic degradation of amoxicillin from aqueous solutions by titanium dioxide nanoparticles loaded on graphene oxide. *Environ. Sci. Pollut. Res.* **28**, 49743–49754. https://doi.org/10.1007/s11356-021-13525-1 (2021).
8. Al-Musawia, T. J. et al. Enhanced sonophotocatalytic degradation of amoxicillin antibiotics using Fe3O4@SiO2/PAEDTC surrounded by MIL-101(Fe) in aquatic environment under the COVID-19 pandemic. *J. Photochem. Photobiol. A* **446**, 115140. https://doi.org/10.1016/j.jphotochem.2023.115140 (2024).
9. Sadughi, M. M. et al. Synthesis of magnetic nanocomposites based on ımidazole zeolite-8 framework doped with silver nanoparticles for effective removal of norfloxacin from effluent. *J. Cluster Sci.* **35**, 2991–3009. https://doi.org/10.1007/s10876-024-02707-9 (2024).
10. Al-Musawia, T. J., Bahramib, P., Rahimpoorc, R., Mengelizadehd, N. & Balarak, D. Enhanced photocatalytic degradation of ciprofloxacin antibiotics using Fe3O4-SiO2-EN@Zn-Al layered double hydroxide nanocomposites under the COVID-19 pandemic. *Results Eng.* **24**, 103396. https://doi.org/10.1016/j.rineng.2024.103396 (2024).
11. Yilmaz, M. et al. Synthesis of activated carbon from Lemna minor plant and magnetized with iron (III) oxide magnetic nanoparticles and its application in removal of Ciprofloxacin. *Biomass Convers. Biorefinery* **14**, 649–662. https://doi.org/10.1007/s13399-021-02279-y (2024).
12. Xu, L. et al. Occurrence, fate, and risk assessment of typical tetracycline antibiotics in the aquatic environment: A review. *Sci. Total Environ.* **753**, 141975. https://doi.org/10.1016/j.scitotenv.2020.141975 (2021).
13. Mukherjee, D. et al. Critical perspectives on metal-organic frameworks and their composites for the adsorptive removal of antibiotics from wastewater matrices. *Cryst. Growth Des.* **23**(11), 7612–7634. https://doi.org/10.1021/acs.cgd.3c00892 (2023).
14. Liao, Q. et al. Interaction between tetracycline and microorganisms during wastewater treatment: A review. *Sci. Total Environ.* **757**, 143981. https://doi.org/10.1016/j.scitotenv.2020.143981 (2021).
15. Pan, S.-F. et al. Separation of tetracycline from wastewater using forward osmosis process with thin film composite membrane—Implications for antibiotics recovery. *Sep. Purif. Technol.* **153**, 76–83. https://doi.org/10.1016/j.seppur.2015.08.034 (2015).
16. Köktaş, İY., Gökkuş, Ö., Kariper, İA. & Othmani, A. Tetracycline removal from aqueous solution by electrooxidation using ruthenium-coated graphite anode. *Chemosphere* **315**, 137758. https://doi.org/10.1016/j.chemosphere.2023.137758 (2023).
17. Balakrishnan, A., Chinthala, M., Polagani, R. K. & Vo, D. N. Removal of tetracycline from wastewater using g-C3N4 based photocatalysts: A review. *Environ. Res.* **216**(Pt 3), 114660. https://doi.org/10.1016/j.envres.2022.114660 (2023).
18. Wang, T. et al. Adsorptive removal of antibiotics from water using magnetic ion exchange resin. *J. Environ. Sci.* **52**, 111–117. https://doi.org/10.1016/j.jes.2016.03.017 (2017).
19. Zhao, L. et al. Removal of tetracycline by ultraviolet/sodium percarbonate (UV/SPC) advanced oxidation process in water. *Environ. Res.* **247**, 118260. https://doi.org/10.1016/j.envres.2024.118260 (2024).
20. Chang, P.-H., Li, Z., Jiang, W.-T., & Sarkar, B. Chapter 7—Clay minerals for pharmaceutical wastewater treatment. In *Modified Clay and Zeolite Nanocomposite Materials* (eds. Mercurio, M., Sarkar, B., & Langella, A.) 167–196. https://doi.org/10.1016/B978-0-12-814617-0.00011-6 (2019).

21. Laabd, M. et al. A novel mesoporous Hydroxyapatite@Montmorillonite hybrid composite for high-performance removal of emerging Ciprofloxacin antibiotic from water: Integrated experimental and Monte Carlo computational assessment. *J. Mol. Liq.* **338**, 116705. https://doi.org/10.1016/j.molliq.2021.116705 (2021).
22. Li, N., Tao, K., Xia, W., Yu, C. & Yang, H. A novel cellulose/lignin/montmorillonite ternary hybrid aerogel for efficiently adsorptive removal of antibiotics from water. *Chem. Eng. J.* **466**, 143265. https://doi.org/10.1016/j.cej.2023.143265 (2023).
23. Liang, G. et al. Efficient removal of oxytetracycline from aqueous solution using magnetic montmorillonite-biochar composite prepared by one step pyrolysis. *Sci. Total Environ.* **695**, 133800. https://doi.org/10.1016/j.scitotenv.2019.133800 (2019).
24. Ma, J. et al. Adsorption properties, kinetics & thermodynamics of tetracycline on carboxymethyl-chitosan reformed montmorillonite. *Int. J. Biol. Macromol.* **124**, 557–567. https://doi.org/10.1016/j.ijbiomac.2018.11.235 (2019).
25. Kryuchkova, M. et al. Pharmaceuticals removal by adsorption with montmorillonite nanoclay. *Int. J. Mol. Sci.* **22**(18), 18. https://doi.org/10.3390/ijms22189670 (2021).
26. po-hsiang, C., Li, Z., Jiang, W.-T., Kuo, C.-Y., & Jean, J.-S.,. Adsorption of tetracycline on montmorillonite influence of solution pH, temperature, and ionic strength. *Desalin. Water Treat.* **55**, 1380–1392 (2015).
27. Xiong, W. et al. Adsorption of tetracycline antibiotics from aqueous solutions on nanocomposite multi-walled carbon nanotube functionalized MIL-53(Fe) as new adsorbent. *Sci. Total Environ.* **627**, 235–244. https://doi.org/10.1016/j.scitotenv.2018.01.249 (2018).
28. Sun, Y. et al. Adsorptive removal of dye and antibiotic from water with functionalized zirconium-based metal organic framework and graphene oxide composite nanomaterial Uio-66-(OH)2/GO. *Appl. Surf. Sci.* **525**, 146614. https://doi.org/10.1016/j.apsusc.2020.146614 (2020).
29. Mahmoud, M. E., Amira, M. F., Seleim, S. M. & Mohamed, A. K. Metal-organic framework-functionalized copper-amine complex: a robust nanocomposite for doxycycline antibiotic removal. *J. Chem. Eng. Data* https://doi.org/10.1021/acs.jced.0c00112 (2020).
30. Singh, N. & Thakur, A. Applications of copper based metal organic frameworks. *Mater. Today Proc.* **50**, 1906–1911. https://doi.org/10.1016/j.matpr.2021.09.264 (2022).
31. Nehra, M., Madan, R. & Dilbaghi, N. Controlled synthesis of Cu-MOF possessing high peroxidase-mimetic activity for colorimetric detection of tetracycline in aqueous solution. *N. J. Chem.* https://doi.org/10.1039/D3NJ00218G (2023).
32. Sadrnia, A. et al. Developing a simple box–behnken experimental design on the removal of doxorubicin anticancer drug using Fe3O4/graphene nanoribbons adsorbent. *Environ. Res.* **200**, 111522. https://doi.org/10.1016/j.envres.2021.111522 (2021).
33. Gulen, B. & Demircivi, P. Adsorption properties of flouroquinolone type antibiotic ciprofloxacin into 2:1 dioctahedral clay structure: Box-Behnken experimental design. *J. Mol. Struct.* **1206**, 127659. https://doi.org/10.1016/j.molstruc.2019.127659 (2020).
34. El Ouardi, M. et al. Efficient removal of p-nitrophenol from water using montmorillonite clay: Insights into the adsorption mechanism, process optimization, and regeneration. *Environ. Sci. Pollut. Res. Int.* **26**(19), 19615–19631. https://doi.org/10.1007/s11356-019-05219-6 (2019).
35. Yang, S. et al. Competitive sorption and selective sequence of Cu(II) and Ni(II) on montmorillonite: Batch, modeling, EPR and XAS studies. *Geochim. Cosmochim. Acta* **166**, 129–145. https://doi.org/10.1016/j.gca.2015.06.020 (2015).
36. Abdelmoaty, A., El-Beih, A. & Hanna, A. Synthesis, characterization and antimicrobial activity of copper-metal organic framework (Cu-MOF) and its modification by melamine. *J. Inorg. Organomet. Polym Mater.* **32**, 1–8. https://doi.org/10.1007/s10904-021-02187-8 (2022).
37. Zdravkov, B., Čermák, J., Šefara, M. & Janků, J. Pore classification in the characterization of porous materials: A perspective. *Open Chem.* https://doi.org/10.2478/s11532-007-0017-9 (2007).
38. Rahman, M. M. et al. Study on optimum IUPAC adsorption isotherm models employing sensitivity of parameters for rigorous adsorption system performance evaluation. *Energies* **14**(22), 7478. https://doi.org/10.3390/en14227478 (2021).
39. Kumar, K. V. et al. Characterization of the adsorption site energies and heterogeneous surfaces of porous materials. *J. Mater. Chem. Mater.* **7**, 10104–10137. https://doi.org/10.1039/c9ta00287a (2019).
40. Fil, B., Özmetin, C. & Korkmaz, M. Characterization and electrokinetic properties of montmorillonite. *Bull. Chem. Commun.* **46**, 258–263 (2014).
41. Salama, R., Abd El-Hakam, S., Samra, S., El-Dafrawy, S. & Ahmed, A. Adsorption, equilibrium and kinetic studies on the removal of methyl orange dye from aqueous solution by the use of copper metal organic framework (Cu-BDC). *Int. J. Mod. Chem.* **10**(2), 195–207 (2018).
42. Obaid, S. A. Langmuir, Freundlich and Tamkin adsorption isotherms and kinetics for the removal Aartichoke Tournefortii straw from agricultural waste. *J. Phys: Conf. Ser.* **1664**(1), 012011. https://doi.org/10.1088/1742-6596/1664/1/012011 (2020).
43. Ahmadpour, A. et al. Dual-purpose magnetic κ-carrageenan/montmorillonite hydrogel for carrying and removal of tetracycline from aqueous medium. *Inorg. Chem. Commun.* **156**, 111274. https://doi.org/10.1016/j.inoche.2023.111274 (2023).
44. Ehsani, A., Aghdasinia, H., Farshchi, M. E., Rostamnia, S. & Khataee, A. Synthesis of sodium alginate/carboxy-methyl cellulose/Cu-based metal-organic framework composite for adsorption of tetracycline from aqueous solution: Isotherm, kinetic and thermodynamic approach. *Surf. Interfaces* **36**, 102506. https://doi.org/10.1016/j.surfin.2022.102506 (2023).
45. Edet, U. & Ifelebuegu, A. Kinetics, isotherms, and thermodynamic modeling of the adsorption of phosphates from model wastewater using recycled brick waste. *Processes* **8**, 665. https://doi.org/10.3390/pr8060665 (2020).
46. Zhao, Y., Gu, X., Li, S., Han, R. & Wang, G. Insights into tetracycline adsorption onto kaolinite and montmorillonite: Experiments and modeling. *Environ. Sci. Pollut. Res. Int.* **22**(21), 17031–17040. https://doi.org/10.1007/s11356-015-4839-2 (2015).
47. Parolo, M. E., Savini, M. C., Vallés, J. M., Baschini, M. T. & Avena, M. J. Tetracycline adsorption on montmorillonite: pH and ionic strength effects. *Appl. Clay Sci.* **40**(1), 179–186. https://doi.org/10.1016/j.clay.2007.08.003 (2008).
48. Cottet, L. et al. Adsorption characteristics of montmorillonite clay modified with iron oxide with respect to methylene blue in aqueous media. *Appl. Clay Sci.* **95**, 25–31. https://doi.org/10.1016/j.clay.2014.03.023 (2014).
49. Kim, N. et al. Effective sequestration of tetracycline and ciprofloxacin from aqueous solutions by Al-based metal organic framework and reduced graphene oxide immobilized alginate biosorbents. *Chem. Eng. J.* **450**, 138068. https://doi.org/10.1016/j.cej.2022.138068 (2022).
50. Saleh, T. A. Chapter 3—Kinetic models and thermodynamics of adsorption processes: Classification. In *Interface Science and Technology*, vol. 34 (ed. Saleh, T. A.) 65–97. https://doi.org/10.1016/B978-0-12-849876-7.00003-8 (2022).
51. Ebelegi, A., Nimibofa, A. & Donbebe, W. Interpretation of adsorption thermodynamics and kinetics. *Open J. Phys. Chem.* **10**, 166–182. https://doi.org/10.4236/ojpc.2020.103010 (2020).
52. Park, J. H., Saravanakumar, G., Kim, K. & Kwon, I. C. Targeted delivery of low molecular drugs using chitosan and its derivatives. *Adv. Drug Deliv. Rev.* **62**(1), 28–41. https://doi.org/10.1016/j.addr.2009.10.003 (2010).
53. Khan, M. A., Kim, S., Rao, R. A. K., Abou-Shanab, R. & a. I., Bhatnagar, A., Song, H., & Jeon, B.-H.,. Adsorption studies of Dichloromethane on some commercially available GACs: Effect of kinetics, thermodynamics and competitive ions. *J. Hazard. Mater.* **178**(1–3), 963–972. https://doi.org/10.1016/j.jhazmat.2010.02.032 (2010).

Acknowledgements

This work was supported by the Istanbul Technical University (ITU) Scientific Research Projects Unit [Grant # MYL-2022-44158].

Author contributions

E.T. made substantial contributions to the conception or design of the work; made substantial contributions to the acquisition, analysis, or interpretation of data; made substantial contributions to have drafted the work; have approved the submitted version; have agreed both to be personally accountable for the author's own contributions and to ensure that questions related to the accuracy or integrity of any part of the work, even ones in which the author was not personally involved, are appropriately investigated, resolved, and the resolution documented in the literature. N.K. made substantial contributions to the conception or design of the work; made substantial contributions to the acquisition, analysis, or interpretation of data; made substantial contributions to have drafted the work; have approved the submitted version; have agreed both to be personally accountable for the author's own contributions and to ensure that questions related to the accuracy or integrity of any part of the work, even ones in which the author was not personally involved, are appropriately investigated, resolved, and the resolution documented in the literature. T.H.S. made substantial contributions to the conception or design of the work; made substantial contributions to the acquisition, analysis, or interpretation of data; made substantial contributions to have drafted the work; have approved the submitted version; have agreed both to be personally accountable for the author's own contributions and to ensure that questions related to the accuracy or integrity of any part of the work, even ones in which the author was not personally involved, are appropriately investigated, resolved, and the resolution documented in the literature. P.D. made substantial contributions to the conception or design of the work; made substantial contributions to the acquisition, analysis, or interpretation of data; made substantial contributions to have drafted the work; have approved the submitted version; have agreed both to be personally accountable for the author's own contributions and to ensure that questions related to the accuracy or integrity of any part of the work, even ones in which the author was not personally involved, are appropriately investigated, resolved, and the resolution documented in the literature. G.N.S. made substantial contributions to the conception or design of the work; made substantial contributions to have substantively revised work; have approved the submitted version; have agreed both to be personally accountable for the author's own contributions and to ensure that questions related to the accuracy or integrity of any part of the work, even ones in which the author was not personally involved, are appropriately investigated, resolved, and the resolution documented in the literature. N.E.A. made substantial contributions to the conception or design of the work; made substantial contributions to have substantively revised work; have approved the submitted version; have agreed both to be personally accountable for the author's own contributions and to ensure that questions related to the accuracy or integrity of any part of the work, even ones in which the author was not personally involved, are appropriately investigated, resolved, and the resolution documented in the literature.

Competing interests

The authors declare no competing interests.

Additional information

Correspondence and requests for materials should be addressed to N.E.-A.

Reprints and permissions information is available at www.nature.com/reprints.

Publisher's note Springer Nature remains neutral with regard to jurisdictional claims in published maps and institutional affiliations.